Spectral CT reconstruction with anti-correlated noise model and joint prior

Mats Persson* and Jonas Adler*

***Abstract*—Spectral CT allows reconstructing a set of material-selective basis images which can be used for material quantification. These basis images can be reconstructed independently of each other or treated as a joint reconstruction problem. In this work, we investigate the effect of two ways of introducing coupling between the basis images: using an anti-correlated noise model and regularizing the basis images with a joint prior. We simulate imaging of a FORBILD Head phantom with an ideal photon-counting detector and reconstruct the resulting basis sinograms with and without these two kinds of coupling. The results show that the anti-correlated noise model gives better spatial resolution than the uncorrelated noise model at the same noise level, but also introduces artifacts. If anti-correlations are introduced also in the prior, these artifacts are reduced and the resolution is improved further.**

I. Introduction

A recent development of Computed Tomography (CT) technology is spectral CT, where transmission data is measured in more than one energy channel. This can be implemented as dual energy CT, which is available today [1]–[3], or as photon-counting CT [4]–[10] which is not yet clinically available. However, how spectral CT data should be reconstructed in order to yield images of optimal clinical value is still only partially understood.

A common way of treating spectral CT data is to perform so-called basis material decomposition. [11] This builds on the observation that the energy-dependent linear attenuation coefficient $\mu(E)$ of any material in the human body can be expressed as a linear combination of two basis functions, $f_1(E)$ and $f_2(E)$: $\mu(E) = a_1 f_1(E) + a_2 f_2(E)$. If a heavy element, such as iodine, is present in the body, its linear attenuation coefficient must be added as a third basis function. The objective of basis material decomposition is then to obtain a basis image, i.e. a map of the basis coefficient a_i, for each $i = 1, \ldots, M$, where M is the number of basis functions (typically 2 or 3). These basis images can be displayed to the radiologist as-is or combined to form a beam-hardening-free monoenergetic image.

A theoretically appealing way to obtain the basis images is by so-called one-step inversion [12], [13], where the basis images are estimated directly from the measured data, e.g. by iteratively solving a maximum a posteriori (MAP) problem. However this approach is computationally challenging since the forward model is nonlinear.

A more easily implementable approach is to divide the reconstruction into two steps: In the first step, projection-based basis material decomposition is used to estimate the line integrals $A_i(\ell) = \int_\ell a_i \mathrm{d}\ell$ of the basis coefficients a_i, $i = 1, \ldots, M$, along each of the sampled projection lines separately. This yields a set of M sinograms of basis projections. In the second step, basis images are reconstructed from these sinograms, either with filtered back-projection [11], [14] or with an iterative method [15]–[18], to yield M basis images.

The simplest such iterative reconstruction algorithms treat the different basis images independently. However, there are potential benefits to be gained from introducing coupling between the reconstruction problems for different basis images. Such coupling can be achieved by including anti-correlations in the noise model. The noise in basis sinograms is anti-correlated between the different basis images, and several authors have reported that including these anti-correlations in the noise model of a MAP problem can reduce noise in the resulting basis images [18]–[21]. In [21] it was demonstrated that this gives rise to cross-talk so that an edge in one basis image can cause an artifact in another basis image.

Another way of introducing coupling between the different basis images is by regularizing with a joint prior. This allows introducing the prior information that image borders in the different basis images should be located in the same place for different basis functions, which is a reasonable assumption in many situations. This has been done previously for energy selective images using matrix rank [15] and for basis images using total nuclear variation [16], structured total variation [22] and a joint edge-preserving regularizer [23].

The purpose of this work is to investigate the effect of combining a coupled noise model with a joint edge-preserving regularizer (prior) in the image domain. We investigate how each of these two types of coupling affects the image noise and whether they cause artifacts or not.

II. Methods

An energy-dependent version of the FORBILD Head phantom [24] was constructed by assigning the attenuation coefficient of soft tissue to the brain, that of the eye lens to the eyes, that of blood to the hematoma and that of cortical bone to the skeleton, all obtained from [25] and [26]. The central ventricle was assigned the same attenuation coefficient as water but rescaled to density 1.045 $\mathrm{g/cm^3}$. An axial slice through $z = 0$ was used.

The CT acquisition simulation was made in a fan-beam geometry with a linear detector array and 500 mm source-

M. Persson was with the Department of Physics, KTH Royal Institute of Technology, SE-100 44, Stockholm, Sweden. He is now with the department of Bioengineering, Stanford University, Stanford, CA 94305. e-mail: mats.persson@mi.physics.kth.se.

J. Adler is with the Department of Mathematics, KTH Royal Institute of Technology, SE-106 91, Stockholm, Sweden, and Elekta Instrument AB, Kungstensgatan 18, SE-103 93 Stockholm, Sweden, e-mail: jonasadl@kth.se

* The authors contributed equally to this work.

 DOI: 10.12059/Fully3D.2017-11-3203027

to-isocenter distance. The detector has 853 detector elements with 0.5 mm spacing in isocenter, and a full (360°) rotation divided into 360 views was simulated.

To generate the data, maps of each material in the phantom were forward projected. To minimize the effect of discretization and inverse crime on the resulting sinograms, this initial forward projection was made using high resolution (8530 detector elements and 3600 angles) and then binned to the resolution used for the reconstruction. These sinograms were used to calculate the energy-dependent attenuation and the expected number of counts λ_j in each energy bin of an ideal photon-counting detector as $\lambda_j = \int_{T_j}^{T_{j+1}} S(E) \exp\left(-\int_\ell \mu(E) \mathrm{d}\ell\right) \mathrm{d}E$ where T_j is energy threshold j and S(E) is the number of incident photons per energy. Eight energy bins were used, with thresholds at 10, 33.2, 40, 50, 60, 70, 80 and 90 keV. Poisson distributed counts were generated from these expected values.

A bowtie filter was simulated by letting the x-ray spectrum S(E) vary with detector position. The filter was constructed from measurements of the dose rate as function of fan angle on a GE VCT scanner with medium field of view. The measured dose profile can be found in [9], and the bowtie thickness profile was calculated in the same way as in Fig. 3a of that publication with the exception that the bowtie material is taken to be Teflon in the present work and that the x-ray spectrum model from [27] (120 kVp, 7° W anode) is used. In the center, where the bowtie filter is thinnest, the half-value layer of the beam is 6.7 mm Al and the number of photons per detector element and each of the 360 binned view angles is 10^6.

From the resulting set of energy bin sinograms, two sinograms of basis projections A_1 and A_2 were calculated using maximum-likelihood basis material decomposition applied to each projection line separately [14]. The linear attenuation coefficients of soft tissue and bone were used as basis functions.

To be able to model the noise accurately in the reconstruction algorithm, the covariance matrix of the bin images must be known. This matrix was estimated to be equal to the Cramér-Rao lower bound (CRLB) [28], which is given by the matrix inverse of the Fisher matrix with elements $F_{ik} = \sum_{j=1}^{N} \frac{1}{\lambda_j} \frac{\partial \lambda_j}{\partial A_i} \frac{\partial \lambda_j}{\partial A_k}$ for independent Poisson distributed counts in N bins with expected values λ_j, $j = 1, \ldots, N$. To mimic a real imaging situation where the ground truth is not available, the CRLB was approximated by replacing the expected counts λ_i in the expression for the Fisher matrix with the Poisson distributed registered counts N_i in each projection line and by using the estimated basis projections A_i resulting from basis material decomposition.

Basis images for soft tissue and bone were reconstructed by solving the optimization problem

$$\min_{\boldsymbol{u} \in \mathcal{X}^M} \|\boldsymbol{A}\boldsymbol{u} - \boldsymbol{b}\|^2_{\boldsymbol{\Sigma}^{-1}} + R(\boldsymbol{u}) \tag{1}$$

where $\boldsymbol{u}$ is a vector containing all image pixel values of both basis images, $\boldsymbol{A}$ is the forward projection operator acting on each component separately and $\boldsymbol{b}$ is the vector of all basis projection estimates in the projection domain for both components. $\boldsymbol{\Sigma}$ is a covariance matrix in the projection domain. Different projection lines are modelled as being independent, but for two basis components in the same projection line, the covariance matrix is given by the CRLB. $\boldsymbol{\Sigma}$ is therefore block diagonal, built up of 2×2 covariance matrices.

For the regularization term $R(\boldsymbol{u})$ we use an edge-preserving joint regularizer. There are several ways to choose such a function. A comprehensive survey of total variation-like joint regularizers for multi-channel images can be found in [29]. Here, we let

$$R(u) = \lambda \int_\Omega \phi(\|[\nabla \boldsymbol{u}](x)\|) dx \tag{2}$$

where $\|\cdot\|$ is a matrix norm and $\nabla \boldsymbol{u}$ is the Jacobian, $[(\nabla \boldsymbol{u})(x)]_{ij} = \left[\frac{\partial u_i}{\partial x_j}\right](x)$. In this article, we investigate weighted Frobenius norms of the form $\|M\|_{\boldsymbol{\Lambda}^{-1}} = \sqrt{\mathrm{Tr}\left(M^T \Lambda^{-1} M\right)}$. ϕ is the Huber penalty function which is quadratic near 0 and linear above a cutoff value [30]:

$$\phi(x) = \begin{cases} \frac{1}{2\sigma} x^2 & \text{if} |x| \le \sigma \\ |x| - \frac{\sigma}{2} & \text{otherwise} \end{cases} \tag{3}$$

This function preserves edges but does not cause the staircasing artifacts that are common in total variation-penalized reconstructions. In this work, $\sigma = 0.005$ was used, which is on the same order of magnitude as the image noise level.

The matrix norm used here has the benefit of being isotropic, meaning that it does not favor gradients in any direction more than others. The matrix $\boldsymbol{\Lambda}$ is a covariance matrix describing prior information on how gradients in the different components are correlated with each other. Here, we use $\boldsymbol{\Lambda} = \left(\begin{smallmatrix} 1 & -c \\ -c & 1 \end{smallmatrix}\right))$ where $c \ge 0$ means that gradients in the two different components are expected to appear at the same places, with opposite signs. This is a reasonable assumption for the present choice of basis functions, since a region containing soft tissue can be expected to begin where a region containing bone ends. The diagonal terms control the influence of each channel and were set to 1 in thus study since we expect approximately equal magnitudes for both channels. If another set of basis materials was used, e.g. soft tissue and a contrast agent, the diagonal values could be set to different magnitudes in order to regularize one channel more than the other.

By solving (1), images were reconstructed both for the $\boldsymbol{\Sigma}$ given by the CRLB (”anti-correlated noise model”) and for $\boldsymbol{\Sigma}$ with off-diagonal terms set to zero (”uncorrelated noise model”). Furthermore, two values for the constant c determining the diagonal terms in $\boldsymbol{\Lambda}$ were tried: $c = 0$ and $c = 0.5$, where the latter value corresponds to a prior assumption that gradients in the two basis images have opposite signs. For comparison, the image was also reconstructed using filtered backprojection (FBP) and by minimizing (1) using either total variation (TV) regularization or the Huber penalty applied independently to each of the two basis functions. For these reconstructions, the projection rays were given constant weight instead of being weighted with the CRLB.

All iterative reconstructions, except for the TV penalty, were performed using the `bfgs_solver` method of ODL[1]. This is an implementation of the limited memory Broyden-Fletcher-Goldfarb-Shanno quasi-newton algorithm [31] implemented

[1] https://github.com/odlgroup/odl

THE 14TH INTERNATIONAL MEETING ON FULLY THREE-DIMENSIONAL IMAGE RECONSTRUCTION IN RADIOLOGY AND NUCLEAR MEDICINE 3

in python. For the TV reconstructions, the Chambolle-Pock method was used instead. 1000 iterations were used in order to ensure convergence. The code used to generate the reconstructions shown in this article is available online[2].

Since different choices of the regularization parameter λ are suitable for the different reconstruction methods, reconstructions were made for a range of values. To be able to compare the resulting images visually, a λ was then selected for each method such that a similar noise level in the soft tissue images was obtained for the different methods.

III. Results

Figure 1 shows the dependence of the noise standard deviation and correlation coefficient $\rho = \mathrm{Cov}(u_{\text{soft tissue}}, u_{\text{bone}})/\sqrt{\mathrm{Var}(u_{\text{soft tissue}}), \mathrm{Var}(u_{\text{bone}})}$. To get similar noise standard deviations in the different soft tissue images (not including FBP), λ was chosen as 5 for the TV prior, 14 for the independent Huber prior, 1.1 for the uncorrelated model with $c = 0$, 1.8 for the anti-correlated model with $c = 0.0$, 1.7 for the uncorrelated model with c=0.5 and 1.5 for the anti-correlated model with $c = 0.5$.

The resulting reconstructed images for these choices of λ are shown in Figure 2. An artifact-prone region of interest (ROI) at the border of the inner ear is shown shown magnified. In the soft tissue images, the magnified inserts are shown with a display window centered on 0 to show the artifacts caused by cross-talk from the bone image. Figure 3 shows a horizontal slice through the center of this ROI, allowing resolution and artifacts to be compared between the images. Figure 4 shows the noise standard deviations of the bone and soft tissue images in another ROI, in the anterior part of the brain.

IV. Discussion

Figure 1(a-b) shows that the noise level for the different varieties of the proposed method are similar for low values of the regularization parameter λ but falls off with different speed for higher λ. This shows the importance of selecting λ individually for the different methods. Figure 1 shows that the noise is strongly anti-correlated between the basis images for low λ. This anti-correlation stems from the strong anti-correlation between the basis sinograms. With TV and the uncorrelated noise models, these anti-correlations decrease only slowly with increasing regularization strength. However, when the anti-correlations are included in the noise model, they are strongly depressed for $\lambda > 0$. If the prior does not include diagonal terms, the method even overcompensates and introduces positive correlations for some values of λ. When anti-correlations are modelled in the prior as well, the correlation coefficient in the images is close to -0.5, in agreement with the prior.

As seen in Figures 2 and 4, all images reconstructed iteratively have much lower noise than the FBP images and the contours of the eyes are readily detectable. Although λ has been tuned so that the TV image and the four proposed methods have similar noise levels in the soft tissue basis

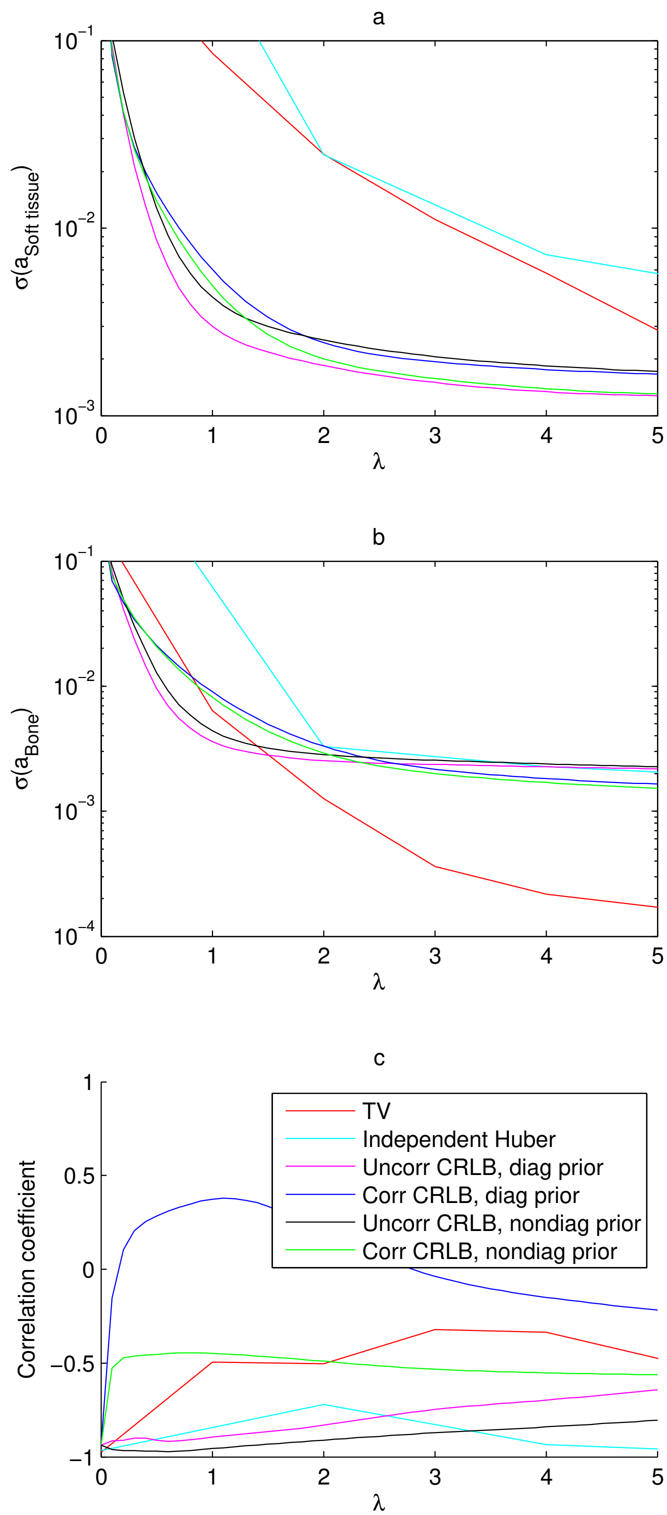

Fig. 1. Standard deviation in the basis images and correlation coefficient between them, measured in the brain tissue ROI (shown as yellow dotted line in Figure 2, as functions of the regularization parameter λ.

[2]https://github.com/adler-j/spectral_ct_examples

THE 14TH INTERNATIONAL MEETING ON FULLY THREE-DIMENSIONAL IMAGE RECONSTRUCTION IN RADIOLOGY AND NUCLEAR MEDICINE 4

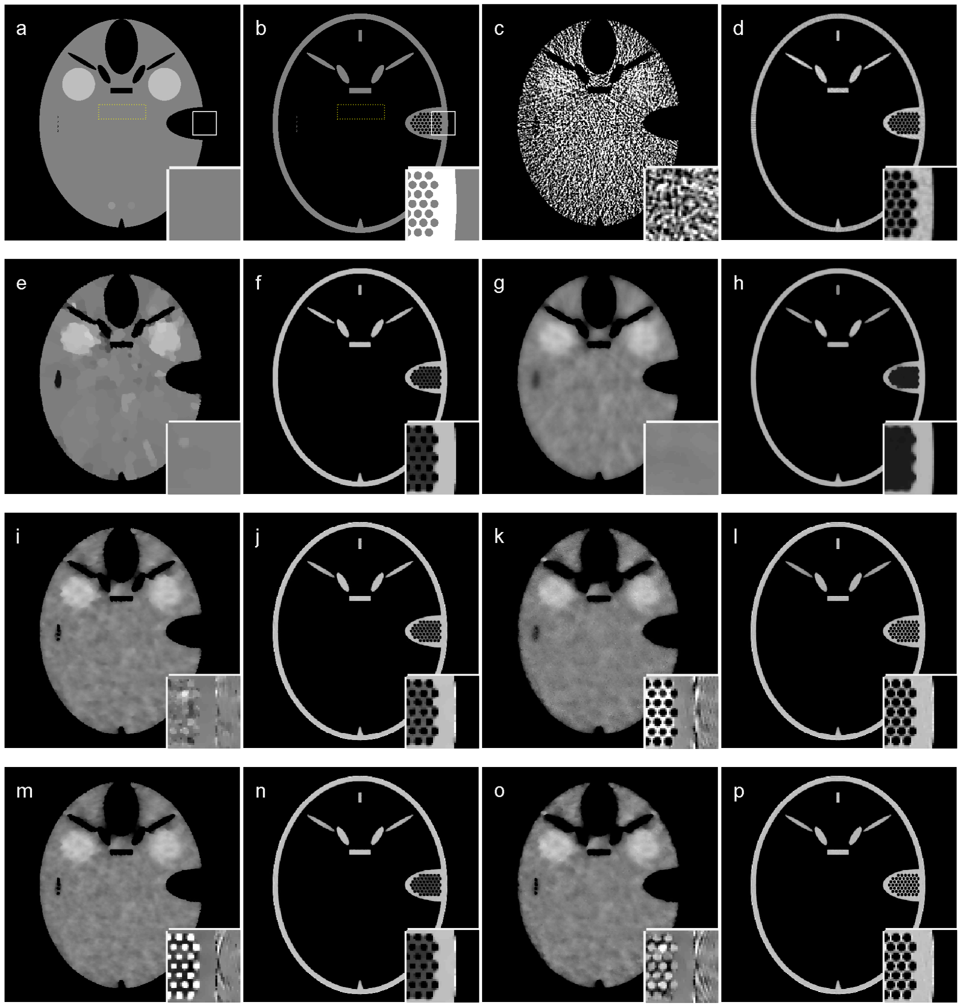

Fig. 2. Reconstructed basis images. Columns 1 and 3 from the left are soft tissue images and the columns 2 and 4 are bone images. (a-b) Ground truth; (c-d) FBP; (e-f) Total variation; (g-h) Independent Huber penalty; (i-j) Proposed method, uncorrelated noise model and c=0; (k-l) Proposed method, anti-correlated noise model and c=1; (m-n) Proposed method, uncorrelated noise model and c=0.5; (o-p) Proposed method, anti-correlated noise model and c=0.5. The ROIs for the noise measurement (yellow dashed rectangle) and for the magnified inserts (white solid rectangle) are shown in the ground truth images. Display window: [0.95 1.05] for soft tissue and [0.4 1.2] for bone. Insert images: [-0.1 0.1] (soft tissue), [0.4 1.2] (bone).

images, the bone image noise differs, with slightly higher noise for the anti-correlated model than the uncorrelated model and close to zero noise in the TV image.

The FBP, TV and independent Huber reconstructions treat the basis images as independent, and therefore these images do not exhibit any artifacts due to cross-talk between basis images. This can be seen on the inner-ear ROIs in Figure 2(a,c,e,g) where the soft tissue images only contain noise. On the other hand, the proposed method, the introduction of coupling in the basis images means that the air bubbles in the bone image can give rise to artifacts in the soft tissue image. With an uncorrelated noise model and $c = 0$ these artifacts are very weak, but some of the air bubbles and the outer border of the skull are visible in the soft tissue image (Figure 2(i)). In this case, the optimization problem is separable in the two basis components as long as the gradient norm $\|\nabla \boldsymbol{u}\|_{\boldsymbol{\Lambda}^{-1}}$ is small, but coupling is introduced by the Huber penalty function ϕ when $\|\nabla \boldsymbol{u}\|_{\boldsymbol{\Lambda}^{-1}}$ is large enough to reach the linear region of ϕ, so that cross-talk may occur at sharp transitions.

Including anti-correlations in the noise model gives strong artifacts in the soft tissue image where the air bubbles are dark like in the bone image (Figure 2(k)). If instead c=0.5, i.e. anti-correlations are assumed in the prior, strong artifacts likewise appear but with inverted contrast, i.e. the air bubbles are bright (Figure 2(m)). Finally, with anti-correlated noise model and c=0.5, the above-mentioned artifacts partially cancel each other, leaving inverted-contrast artifacts of reduced magnitude (Figure 2(o)).

The bone coefficient profiles in Figure 3 shows that the anti-correlated noise model gives higher resolution than the uncorrelated noise model, at similar soft tissue noise level (Figure 4). Changing c from 0 to 0.5 for the uncorrelated noise model leaves resolution unchanged. However, when used with the anti-correlated noise model, $c = 0.5$ gives a slightly sharper bone image than $c = 0$ (Figure 3). This is in line with the intention of improving resolution at interfaces by setting $c > 0$. Despite having similar noise level in the soft tissue basis image, all four variants of the proposed method yield better spatial resolution than the independent Huber method, as can be seen from the high-resolution pattern in the left part of the

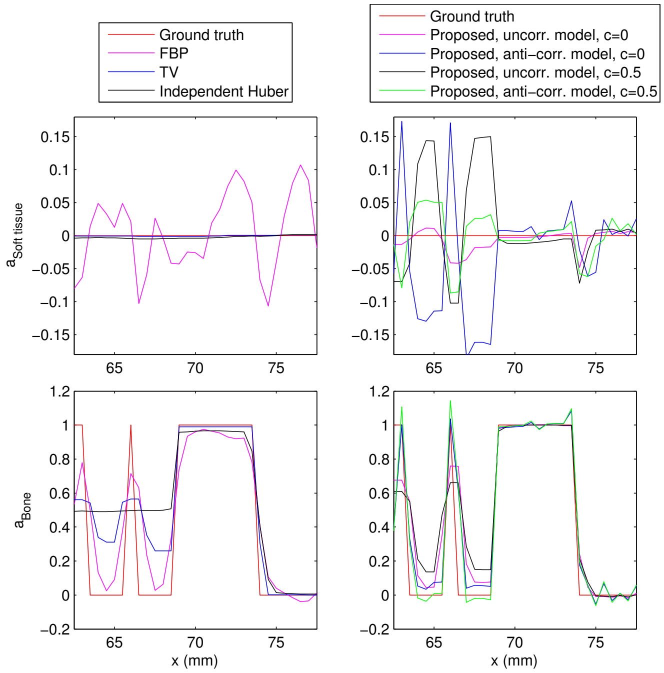

Fig. 3. Horizontal profiles of the basis coefficients for soft tissue and bone through the center of the ROI shown in the inserts of Figure 2 and through the center of one row of air bubbles. The x coordinate is defined relative to the image center. (The different reconstructions are divided into two plots for each basis function, for clarity.)

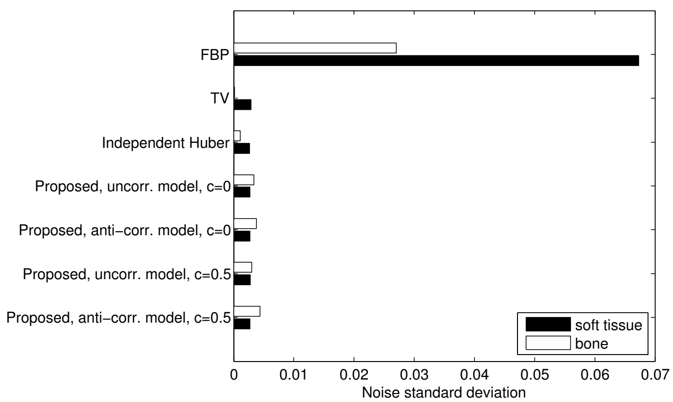

Fig. 4. Noise standard deviation in the brain tissue measured in the ROIs shown as yellow dashed rectangles in Figures 2(a-b).

image and from the air bubbles in the right part. For the images reconstructed with the independent Huber penalty, the fact that the projections are not weighted with the CRLB causes over-regularization of the bone image, leading to a very low noise level but also causes the air-bubble pattern to disappear.

V. Conclusion

Using an anti-correlated noise model gives better resolution than an uncorrelated noise model for equal noise level in the soft-tissue image, but this improvement comes at the cost of artifacts due to cross-talk between basis images. However, if anti-correlations are modelled in the prior as well, these artifacts are reduced and the spatial resolution is further improved.

Acknowledgment

This study was funded by the Erling-persson Family Foundation (Familjen Erling-Perssons stiftelse), NIH Grant U01 EB01714003 and Swedish Foundation for Strategic Research grants Low complexity reconstruction for medicine (AM13-0049) and 3D reconstruction with simulated image formation models (ID14-0055). Funding and data has also been provided by Elekta (Stockholm, Sweden). M. Persson has financial interests in Prismatic Sensors AB.

References

[1] T. R. C. Johnson, B. Krauß, M. Sedlmair, M. Grasruck, H. Bruder, D. Morhard, C. Fink, S. Weckbach, M. Lenhard, B. Schmidt, T. Flohr, M. F. Reiser, and C. R. Becker, "Material differentiation by dual energy CT: initial experience," *Eur. Radiol.*, vol. 17, no. 6, pp. 1510–1517, 2006.

[2] J. Hsieh, "Dual-energy CT with fast-kVp switch," *Medical Physics*, vol. 36, no. 6, pp. 2749–2749, 2009.

[3] R. Carmi, G. Naveh, and A. Altman, "Material separation with dual-layer CT," in *Nuclear Science Symposium Conference Record, 2005 IEEE*, vol. 4, 2005, p. 3.

[4] K. Taguchi and J. S. Iwanczyk, "Vision 20/20: Single photon counting x-ray detectors in medical imaging," *Med. Phys.*, vol. 40, no. 10, p. 100901, 2013.

[5] J. Giersch, D. Niederlöhner, and G. Anton, "The influence of energy weighting on x-ray imaging quality," *Nucl. Instrum. Meth. A*, vol. 531, no. 1–2, pp. 68 – 74, 2004, proceedings of the 5th International Workshop on Radiation Imaging Detectors.

[6] P. M. Shikhaliev, "Energy-resolved computed tomography: first experimental results," *Phys. Med. Biol.*, vol. 53, no. 20, pp. 5595–5613, Oct. 2008.

[7] J. P. Schlomka, E. Roessl, R. Dorscheid, S. Dill, G. Martens, T. Istel, C. Bumer, C. Herrmann, R. Steadman, G. Zeitler, A. Livne, and R. Proksa, "Experimental feasibility of multi-energy photon-counting K-edge imaging in pre-clinical computed tomography," *Phys. Med. Biol.*, vol. 53, no. 15, pp. 4031–4047, Aug. 2008.

[8] J. P. Ronaldson, R. Zainon, N. J. A. Scott, S. P. Gieseg, A. P. Butler, P. H. Butler, and N. G. Anderson, "Toward quantifying the composition of soft tissues by spectral CT with Medipix3," *Med. Phys.*, vol. 39, no. 11, pp. 6847–6857, 2012.

[9] M. Persson, R. Bujila, P. Nowik, H. Andersson, L. Kull, J. Andersson, H. Bornefalk, and M. Danielsson, "Upper limits of the photon fluence rate on ct detectors: Case study on a commercial scanner," *Medical Physics*, vol. 43, no. 7, pp. 4398–4411, 2016.

[10] Z. Yu, S. Leng, S. M. Jorgensen, Z. Li, R. Gutjahr, B. Chen, A. F. Halaweish, S. Kappler, L. Yu, E. L. Ritman, and C. H. McCollough, "Evaluation of conventional imaging performance in a research whole-body CT system with a photon-counting detector array," *Phys. Med. Biol.*, vol. 61, no. 4, p. 1572, 2016.

[11] R. E. Alvarez and A. Macovski, "Energy-selective reconstructions in x-ray computerised tomography," *Phys. Med. Biol.*, vol. 21, no. 5, pp. 733–744, Sept. 1976.

[12] R. F. Barber, E. Y. Sidky, T. G. Schmidt, and X. Pan, "An algorithm for constrained one-step inversion of spectral CT data," *Physics in Medicine and Biology*, vol. 61, no. 10, p. 3784, 2016.

[13] Y. Long and J. A. Fessler, "Multi-material decomposition using statistical image reconstruction for spectral CT," *IEEE Transactions on Medical Imaging*, vol. 33, no. 8, pp. 1614–1626, Aug 2014.

[14] E. Roessl and R. Proksa, "K-edge imaging in x-ray computed tomography using multi-bin photon counting detectors," *Phys. Med. Biol.*, vol. 52, no. 15, p. 4679, 2007.

[15] H. Gao, H. Yu, S. Osher, and G. Wang, "Multi-energy CT based on a prior rank, intensity and sparsity model (PRISM)," *Inverse Problems*, vol. 27, no. 11, p. 115012, 2011.

[16] D. S. Rigie and P. J. L. Rivière, "Joint reconstruction of multi-channel, spectral CT data via constrained total nuclear variation minimization," *Physics in Medicine and Biology*, vol. 60, no. 5, p. 1741, 2015.

[17] C. Schirra, E. Roessl, T. Koehler, B. Brendel, A. Thran, D. Pan, M. Anastasio, and R. Proksa, "Statistical reconstruction of material decomposed data in spectral CT," *Medical Imaging, IEEE Transactions on*, vol. 32, no. 7, pp. 1249–1257, July 2013.

[18] R. Zhang, J. B. Thibault, C. A. Bouman, K. D. Sauer, and J. Hsieh, "Model-based iterative reconstruction for dual-energy x-ray CT using a joint quadratic likelihood model," *IEEE Transactions on Medical Imaging*, vol. 33, no. 1, pp. 117–134, Jan 2014.

[19] A. Sawatzky, Q. Xu, C. Schirra, and M. Anastasio, "Proximal ADMM for multi-channel image reconstruction in spectral x-ray CT," *Medical Imaging, IEEE Transactions on*, vol. 33, no. 8, pp. 1657–1668, Aug 2014.

[20] K. M. Brown, S. Zabić, and G. Shechter, "Impact of spectral separation in dual-energy CT with anti-correlated statistical reconstruction," *Proceedings of The thirteenth International Meeting on Fully Three-Dimensional Image Reconstruction in Radiology and Nuclear Medicine, Newport, RI,USA*, 2015.

[21] M. Persson and F. Grönberg, "Spatial-frequency-domain study of anti-correlated noise reduction in spectral CT," in *Proc. 4th Intl. Mtg. on image formation in X-ray CT*, 2016, pp. 283–6.

[22] D. Zeng, Z. Bian, C. Gong, J. Huang, J. He, H. Zhang, L. Lu, Q. Feng, Z. Liang, and J. Ma, "Iterative image reconstruction for multienergy computed tomography via structure tensor total variation regularization," pp. 978 349–978 349–9, 2016.

[23] W. Huh and J. A. Fessler, "Iterative image reconstruction for dual-energy X-ray CT using regularized material sinogram estimates," in *2011 IEEE International Symposium on Biomedical Imaging: From Nano to Macro*, March 2011, pp. 1512–1515.

[24] G. Lauritsch and H. Bruder, "FORBILD head phantom." [Online]. Available: http://www.imp.uni-erlangen.de/forbild/english/results/head/head.html

[25] M. J. Berger, J. H. Hubbell, S. M. Seltzer, J. Chang, J. S. Coursey, R. Sukumar, D. S. Zucker, and K. Olsen, "XCOM: Photon Cross Section Database," http://physics.nist.gov/xcom. National Institute of Standards and Technology, Gaithersburg, MD, 2005.

[26] *Tissue substitutes in Radiation Dosimetry and Measurement (report 44)*. International Commission on Radiation Units and Measurements, Bethesda, MD, 1989.

[27] K. Cranley, B. J. Gilmore, G. W. A. Fogarty, L. Desponds, and D. Sutton. (1997) IPEM report 78: Catalogue of diagnostic x-ray spectra and other data, electronic version. York: IPEM.

[28] E. Roessl and C. Herrmann, "Cramér-Rao lower bound of basis image noise in multiple-energy x-ray imaging," *Physics in Medicine and Biology*, vol. 54, no. 5, p. 1307, 2009.

[29] J. Duran, M. Moeller, C. Sbert, and D. Cremers, "Collaborative total variation: A general framework for vectorial TV models," *SIAM Journal on Imaging Sciences*, vol. 9, no. 1, pp. 116–151, 2016.

[30] J. A. Fessler, "Grouped coordinate descent algorithms for robust edge-preserving image restoration," *Proc. SPIE*, vol. 3170, pp. 184–194, 1997.

[31] D. C. Liu and J. Nocedal, "On the limited memory BFGS method for large scale optimization." *Math. Program.*, vol. 45, no. 1-3, pp. 503–528, 1989.